Phase-field modeling of elastic-plastic fracture propagation in punch through shear test

M. Jarrahi[1], G. Blöcher[2], and C. Kluge[2], and H. M. Holländer[1]

[1]Department of Civil Engineering, University of Manitoba, Winnipeg, Canada.

[2]Helmholtz Centre Potsdam - GFZ German Research Centre for Geosciences.

Corresponding author: Miad Jarrahi (jarrahim@myumanitoba.ca)

Key Points:

- Crack Phase-field method is applied to model the solid fracturing.
- Elastic-plastic fracturing is numerically simulated.
- The method is implemented on Punch Through Shear testing to calculate the Mode II fracture toughness.

Abstract

Fracture initiation and propagation from a wellbore within a rock formation exhibit nonlinear and inelastic behaviors. When the rock material undergoes plastic deformation prior to failure, the classical Griffith theory is no longer valid. In this study, a variational phase-field approach is applied to model the inelastic behavior of granite rock in a punch through shear test. The rock failure and the fracture initiation and propagation during the loading was simulated and compared to the corresponding experimental investigations. In this numerical approach, the total local free energy is fully coupled with solid deformation and computes the plastic strain rate. The code is scripted in Multiphysics Object Oriented Simulation Environment (MOOSE). The model is shown capable of reproducing the three point bending benchmark problem and the evidenced phenomena from Punch Through Shear (PTS) test encompassing mixed mode fracture pattern (Mode I, and Mode II), and wing fractures. The numerical results show a good agreement in stress-displacement curve with experimental data for critical energy release rate of $G_c = 600\ \mathrm{N/m}$. Therefore, the granite sample's fracture toughness for Mode II is calculated to be 4.85 $\mathrm{MPa}\sqrt{\mathrm{m}}$ at no confining pressure.

1 Introduction

In geologic formations, the rock deformation occurs due to tectonic plate movement (Lei & Wang, 2016) or human activities such as hydraulic fracturing (Speight, 2016). The rock deformation can be characterized based on the rock material, the temperature, and different stress states. Based on the stress state the rock can either deform in tensile mode (Mode I), where the rock element is stretched, compressional mode, where the rock element is compressed, and the shear mode (Mode II), where a side to side shearing is exerted on the rock element. The rock deformation in response to deviatoric stresses may undergo an elastic deformation or rock failure.

The subject of rock failure was studied since 1960s by examination of natural rock formations or laboratory experiments on core rock samples through in-situ tests or by rock excavation during engineering construction (Tang & Hudson, 2010). Accordingly, the rock failure is placed between two extreme situations; pure brittle fracture and pure ductile fracture (Zhang, 2010).

Ductile fracture (plastic fracture) is a fracture of rocks undergoing plastic deformation prior to failure (Pineau & Besson, 2001). Rice (1968) proposed the basic elastic–plastic fracture mechanics approach with a path independent J-integral. Elices and Liorca (2002) reported a tensile stress test that the material eventually reaches the point that rate of strain hardening is less than the loss in cross-sectional area, so that it forms the necked region. They evidenced that within the necked region, a central crack is nucleated radially and propagated along localized shear planes at 45° to the axis, to form a cup-and-cone ductile fracture after a tensile test. Therefore, a ductile fracture presents three different zones including a fibrous, a radial, and a shear lip zone (Affonso, 2006). A fibrous zone is a region where the fracture initiates and propagates stably at the onset of the highest stress tri-axiality (i.e. the ratio of lithostatic stress to the von Mises equivalent stress) (Affonso, 2006; Nam, Kim, Han, Kim, & Kim, 2014). A region with a rough surface, with unstable fracture propagation, corresponds to the radial zone. A shear lip zone is a region with a 45° of inclination from the external load direction, where the stress tri-axiality is reduced (Affonso, 2006). Moreover, Mouritz (2012) is stated that, the stress distribution ahead of a ductile fracture is uneven and forms the elastic and plastic zone. The local

stress increases as it gets closer to the crack tip (i.e. singularity within the J-integral path (Karihaloo & Xiao, 2003)). At a certain distance from the crack tip, the local stress approaches the yield stress σ_y of the rock. Therefore, the rock deformation within that distance from the crack tip is plastic and the region is called the plastic zone. Outside the plastic zone, the rock is stressed below the yield strength and, thus, deforms elastically and the region is called elastic zone (Mouritz, 2012). The formation of crack tip plastic zone is energy absorbent. Thus, the applied stress needed to cause crack growth increases with the length of the fracture. This behavior makes ductile fracture more difficult to grow to the critical size which causes failure in the rock (Mouritz, 2012).

The computational modeling of plastic fracturing is expected to predict the plastic deformation in crack tip plastic zone other than the elastic zone deformation, and fracture propagation.

Several studies have focused on numerical simulation of ductile fracture, see Besson (2009) for a comprehensive review. It was stated that the Rice`s J-integral approach has some major issues such as: i) the crack initiation and propagation from a stress concentrator cannot be predicted, ii) the critical value for j-integral as a fracturing criterion is not a material property and depends on the geometry and loading boundary condition. The same drawbacks were seen in criteria such as critical Crack Tip Opening Displacement (CTOD) (Davies & Wells, 1961), and Crack Tip Opening Angle (CTOA) (Dawicke, Piascik, & Newman, 1997; James & Newman, 2003; Mahmoud & Lease, 2003). For example, the critical CTOA was shown to decrease with increasing sample thickness, while it was bounded to lower and higher values (Mahmoud & Lease, 2003). Bouchard, Bay, and Chastel (2003) implemented other fracturing criteria such as the maximal circumferential stress criterion (MCSC) (McClintock, 1963), the Minimum Strain Energy Density Criterion (MSEDC) (Maiti & Smith, 1984), and the criterion of the Maximal Strain Energy Release Rate (MSERR) (Hussain, Pu, & Underwood, 1974), using advanced finite element remeshing and nodal relaxation techniques. They showed that, MSEDC is less accurate than two other criteria. The MCSC requires mesh refinement at the crack tip so that the results might be influenced by the mesh structure. Finally, they concluded that the accuracy of MSERRC is mesh-independent and provides good results for brittle fracturing. Each of these criteria were implemented through finite element remeshing technique, where a real mesh discontinuity represented the fracture and the walls of the fracture were considered as the moving boundaries within the computational domain.

Generally, fracture propagation models can be classified into discrete and continuous approaches. Discrete methods compute the sudden changes in the displacement field and introduce them as discontinuities. Among those are the extended finite element method (Sukumar, Moës, Moran, & Belytschko, 2000), cohesive elements, element-erosion techniques (Johnson & Stryk, 1987), and remeshing techniques (Areias, Rabczuk, & Msekh, 2016; Bouchard et al., 2003).

Discrete fracture methods require complicated procedures to track the fractures. In rock engineering and rock fracture, it is important to study the fluid flow within the fracture, especially in hydraulic fracturing, where a rock formation is stimulated by hydraulic forces. However, discrete approaches fail to provide a domain within the fracture to model the fluid flow. Other discrete fracture modeling such as the cracking particle method (Rabczuk & Belytschko, 2004), peridynamics (Madenci & Oterkus, 2014), and dual horizon peridynamics

(Ren, Zhuang, Cai, & Rabczuk, 2016) may have higher accuracy, yet, the fluid flow through the opening of fractures cannot be modeled due to the absence of crack path continuity.

On the other hand, continuous approaches including gradient damage model (Peerlings, DE Borst, Brekelmans, & DE Vree, 1996), screened Poisson models (Areias, Msekh, & Rabczuk, 2016), and phase-field models (C. Miehe, Welschinger, & Hofacker, 2010), introduce an intrinsic length scale as the finite width of the fracture. This may simplify the implementation and provides a continuous opening of the fracture for later fluid flow modeling. Continuous approaches, however, are unable to describe the softening in ductile fracturing (Ambati, Gerasimov, & De Lorenzis, 2015). Typically, the softening and damage localization phase are handled by either the remeshing or the Extended Finite Element Method (XFEM). This led to use of combined discrete and continuous methods such as Gurson–Tvergaard–Needleman (GTN) model (Crété, Longère, & Cadou, 2014) with the XFEM. Accordingly, additional complications arise for a consistent and seamless transition between continuous and discrete fracture descriptions.

Among those continuous methods, phase-field approach was reported to be consistent in modeling sharp interfaces (C. Miehe et al., 2010). In this method, a smooth transition of an order parameter, the crack phase-field from 0 to 1, approximates the sharp fracture discontinuity. The change in the crack phase-field parameter due to the change in stress-strain field models the brittle fracture propagation on a fixed mesh (Bourdin, Francfort, & Marigo, 2000; C. Kuhn & Müller, 2008; Charlotte Kuhn & Müller, 2010; Christian Miehe & Mauthe, 2016; C. Miehe et al., 2010).

The extension of phase-field approach to model the ductile fracturing was studied in Hofacker and Miehe (2012) and Ulmer, Hofacker, and Miehe (2013). In these studies, the total energy is the sum of elastic deformation energy, plastic deformation energy, and fracture energy. The elastic deformation and fracture energy functions are considered as the same as brittle fracture energy function. The plastic deformation energy is defined as a chosen function including plastic fracture mechanics parameters such as the elastic modulus, the yield stress, and the strain hardening exponent. Ambati et al. (2015) presented a phase-field model for ductile fracture, in which the degradation function applied to the tensile portion of the elastic strain energy were coupled to the one applied to the plastic strain energy, to provide higher accuracy than previous phase field approaches. Most recently, Dittmann, Aldakheel, Schulte, Wriggers, and Hesch (2018) proposed a phase-field model based on a triple multiplicative decomposition of the deformation gradient to improve the accuracy of ductile material behavior or Huang and Gao (2019) used a phase-field with the modification of the crack driving force function by including the plastic contribution.

This numerical study is based on the punch through shear test (PTS) that was performed to calculate the Mode II fracture toughness. The PTS-testing was applied to a cylindrical granite sample with the drilled circular notches. The notches provided a friction free initiation locus for fractures. More details of the PTS-testing is described in Backers, Stephansson, and Rybacki (2002). In this paper, we used the total free energy derivatives to compute the evolution of crack phase-field parameter that follows the standard Allen-Cahn equation, where the strain energy density is coupled with plasticity constitutive equation. The distinct benefit of the proposed phase-field model is to facilitate the use of the common feature of all phase-field models, *i.e.* their reliance of total free energy functional, with a material behavior under the loading. For the rock behavior under the loading, the normality hypothesis of plasticity (Dunne & Petrinic,

2005a) is used to compute the stress field when there is inelastic strain. At each time step, the stress field is updated through the strain energy density to ensure the thermodynamically consistency of the model. The code is built on the libMesh finite element library of Multiphysics Object Oriented Simulation Environment (MOOSE) (Gaston et al., 2015), which provides an implicit coupling with an extensive scalable parallel algorithm including parallel adoptive mesh refinement unstructured grids and adoptive time step size. In conclusion, the numerical simulation of the mechanical processes during the PTS testing such as the solid deformation and the fracture initiation and propagation, provided a tool to couple such mechanical processes with the fluid flow and heat transfer in the well-bore and field operations such as hydraulic fracturing and enhanced geothermal reservoirs.

2 Variational phase-field method for elastic-plastic fracturing

The crack phase-field c is defined in a bounded solid domain with an external boundary and an internal discontinuity boundary assumed as the fracture boundary. The fracture topology is a sharp interface between the solid domain (i.e. unbroken material, $c = 0$) and the fracture domain (i.e. fully broken material, $c = 1$). To avoid the discontinuity between unbroken and fully broken material, the regularization crack surface density function $\gamma(c)$ (C. Miehe et al., 2010) is defined to diffuse the fracture topology with the regularized crack phase-field $c \in (0,1)$ over the regularization length of l:

$$\gamma(c) = \frac{1}{2l}c^2 + \frac{l}{2}|\nabla c|^2 \tag{1}$$

2.1 The evolution of crack phase-field

The deformation of diffused fracture surface can be described by the evolution of crack phase-field), where the fracture initiates, propagates in an arbitrary direction, bifurcates, and merges with other existing fractures in the range of $[0, T]$ of time. Because the fracture is energy dissipative in nature (C. Miehe et al., 2010), the irreversibility of the fracturing process is ensured by satisfying a positive changes of crack surface density function with time.

$$\frac{\partial \gamma}{\partial t} := \frac{\partial \gamma}{\partial c}\frac{\partial c}{\partial t} = \left(\frac{1}{l}c - \frac{l^2}{2}\nabla^2 c\right)\frac{\partial c}{\partial t} \geq 0 \tag{2}$$

In this phase-field approach, the fracture energy density function E_f is introduced to ensure the above constraints:

$$E_f = G_c\gamma \tag{3}$$

where G_c is a threshold value of elastic energy release rate in the Griffith theory.

For the solid domain response of a fracture evolution, it is assumed that the fracture only occurs in tension, thus, the energy dissipation is anisotropic. Therefore, the free energy storage density function ψ (accordingly the stress tensor σ) is decomposed into the stored energy density

182 due to tension $\psi^+(\varepsilon)$ (tensile stress component σ_0^+) and due to compression $\psi^-(\varepsilon)$ (compressive
183 stress component σ_0^-) as following
184

$$\psi(\varepsilon(u), c) = ((1-c)^2(1-k)+k)\,\psi^+(\varepsilon) + \psi^-(\varepsilon) \tag{4a}$$

$$\sigma := \frac{\partial\psi(\varepsilon(u), c)}{\partial\varepsilon} = ((1-c)^2(1-k)+k)\,\sigma_0^+ + \sigma_0^- \tag{4b}$$

185

186 and depends on the displacement u and the phase-field c, where ε is the solid strain. The
187 $k \approx 0$ is a small positive parameter for the discretization method to remain well-posed for partly-
188 broken material. Subsequently, the term $k\psi^+(\varepsilon)$ characterizes the artificial elastic rest energy
189 density around the diffused fracture boundary. The stress tensor σ is called cracked stress in the
190 fracturing material, while σ_0 is an imaginary stress called uncracked stress defined in the
191 material with the same boundary condition but without the fracture.

192 Finally, the total free energy density E can be expressed as the summation of fracture
193 energy density (see Eq. 3) and the free energy storage density (see Eq. 4a).
194

$$\mathrm{E}(\varepsilon(\mathrm{u}), \mathrm{c}) = ((1-\mathrm{c})^2(1-k)+k)\psi^+(\varepsilon) + \psi^-(\varepsilon) + G_c\gamma \tag{5}$$

195

196 For the transient computations over the time interval $[0, \mathrm{t}_0]$, where t_0 is the current time
197 step, the fracture only occurs at the maximum stored energy density due to tensile, i.e.
198

$$\mathrm{H} = \max(\psi^+)_{t_0} \tag{6}$$

199

200 Therefore the total free energy is redefined as:
201

$$\mathrm{E}(\varepsilon(\mathrm{u}), \mathrm{c}) = ((1-\mathrm{c})^2 + k)\,\mathrm{H} + \psi^-(\varepsilon) + \frac{1}{2l}G_c(c^2 + l^2|\nabla c|^2) \tag{7}$$

202

203 The evolution of crack phase-field with time takes place at minimum total free energy,
204 which forms the standard Allen-Cahn equation (Allen & Cahn, 1972; Gaston et al., 2015)
205

$$\frac{\partial c}{\partial t} + L\frac{\partial \mathrm{E}(\varepsilon(\mathrm{u}), \mathrm{c})}{\partial \mathrm{c}} = 0 \tag{8}$$

206

207 where L is the mobility. Referring to Eq. (2), (7) and (8), the numerical implementation of the
208 evolution of total free energy density can result the following
209

$$\frac{\partial c}{\partial t} = -L\frac{\partial \mathrm{E}(\varepsilon(\mathrm{u}), \mathrm{c})}{\partial \mathrm{c}} := -L\left(-2(1-c)(1-k)H + G_c\left(\frac{1}{l}c - \frac{l^2}{2}\nabla^2 c\right)\right) \tag{9}$$

210

211

2.2 von Mises Plasticity

Huang and Gao (2019) introduced a phase-field with three phases including 1- the solid domain with elastic deformation, 2- the fracture, and 3- the solid domain with plastic deformation. In this study, we follow the phase-field in C. Miehe et al. (2010) prescribed for elastic solid fracturing. However, the free energy storage density function $\psi(\varepsilon(u), c)$ and the stress state $\sigma(\varepsilon(u), c)$ are modified when the material undergoes a plastic deformation.

The boundary condition of the solid material is prescribed with either the Dirichlet condition, where the displacement is known, or the Neumann condition, where the traction force is known. Therefore, the strain $\varepsilon(u)$ is obtained for the material without the fracture:

$$\varepsilon = \begin{pmatrix} \varepsilon_{xx} & \varepsilon_{xy} & \varepsilon_{xz} \\ \varepsilon_{yx} & \varepsilon_{yy} & \varepsilon_{yz} \\ \varepsilon_{zx} & \varepsilon_{zy} & \varepsilon_{zz} \end{pmatrix} = \begin{pmatrix} \frac{\partial u_x}{\partial x} & \frac{\partial u_x}{\partial y} & \frac{\partial u_x}{\partial z} \\ \frac{\partial u_y}{\partial x} & \frac{\partial u_y}{\partial y} & \frac{\partial u_y}{\partial z} \\ \frac{\partial u_z}{\partial x} & \frac{\partial u_z}{\partial y} & \frac{\partial u_z}{\partial z} \end{pmatrix} \tag{10}$$

According to the classical additive decomposition of strain (Dunne & Petrinic, 2005b), the uncracked stress is obtained by

$$\sigma_0(\varepsilon(u)) = E(\varepsilon - \varepsilon^p) \tag{11}$$

where ε^p is the plastic strain, and E is the Young modulus of the solid material. Here, the uncracked stress state is checked based on the von Mises yield surface function f criterion for the solid material under multiaxial loading condition.

$$f = \sigma_{e,0} - \sigma_y \tag{12}$$

where σ_y is the yeild stress of the solid material, $\sigma_{e,0}$ is the uncracked effective stress in the solid domain, defined as

$$\sigma_{e,0} = \left(\frac{1}{2}(\sigma_{1,0} - \sigma_{2,0})^2 + \frac{1}{2}(\sigma_{2,0} - \sigma_{3,0})^2 + \frac{1}{2}(\sigma_{3,0} - \sigma_{1,0})^2\right)^{\frac{1}{2}} \tag{13}$$

where $\sigma_{1,0}$, $\sigma_{2,0}$, and $\sigma_{3,0}$ are the principal stresses of the material with no fracture. The von Mises yield criterion defines the stress limit at which the material becomes plastic, where the inside of the yield surface $f < 0$ is the elastic stress state, and the boundary $f = 0$ is the stress state with plastic deformations (Dunne & Petrinic, 2005b).

At the conditions necessary to initiate yielding (i.e. $f = 0$), the normality hypothesis of plasticity (Dunne & Petrinic, 2005b) determines that the direction in plastic strain increment tensor $d\varepsilon^p$ is normal to the tangent to the yield surface at the load point and can be obtained by:

$$d\varepsilon^p = dp\frac{\partial f}{\partial \sigma} = \frac{3}{2}\, dp\, \frac{\acute{\sigma}_0}{\sigma_{e,0}} \tag{14}$$

where $\acute{\sigma}_0$ is the deviotoric uncracked stress tensor. Here, $\frac{\partial f}{\partial \sigma}$ gives the direction of the plastic strain increment and dp determines the magnitude of plastic strain increment, that is called plastic multiplier or the effective plastic strain increment. Then, the uncracked stress increment $d\sigma_0$ is obtained using radial return map algorithm.

2.3 The radial return map plasticity algorithm

This algorithm is unconditionally stable, while the accuracy depends on the time step size, Δt.

According to Eq. (11), the uncracked stress can be obtained at the new time step, using the updated plastic strain $\varepsilon^p{}_{t+\Delta t}$.

$$\sigma_{0_{t+\Delta t}} = E\big(\varepsilon_{t+\Delta t} - \underbrace{(\varepsilon^p{}_t + d\varepsilon^p)}_{\varepsilon^p{}_{t+\Delta t}}\big) \tag{15}$$

However, the updated stress needs to be corrected when it is outside of the yield surface (i.e. $f > 0$) as it does not convey a physical meaning. Therefore, $\sigma_{0_{t+\Delta t}}$ is stored as a trial stress σ^{tr} in order to be later corrected by plastic correction to be brought back onto the yield surface. The effective stress required to return the stress onto the yield surface is as follows (Dunne & Petrinic, 2005b):

$$\sigma_e = \sigma_e^{tr} - 3G\Delta p \tag{16}$$

here $G = E/2(1+\nu)$ is the shear modulus for an isotropic material, where ν is the Poisson ratio. In addition, plastic deformation causes the yield surface movement in stress space and this leads to a new yield surface f', defined as

$$f' = f + r \tag{17}$$

where r is the hardening tensor in stress space. Substituting Eq. (16) and (12) into Eq. (17) for stress state in plastic deformation condition, where $f' = 0$, it can be re-written as

$$f' = \sigma_e^{tr} - 3G\Delta p - \sigma_y = 0 \tag{18}$$

Substituting Eq. (18) into the following Newton`s method

$$f + \frac{\partial f}{\partial \Delta p} d\Delta p = 0 \tag{19}$$

Finally, the plastic correction $\mathrm{d}\Delta\mathrm{p}$ and effective plastic strain increment are obtained as

$$d\Delta p = \frac{f}{3G + \frac{\partial r}{\partial \Delta p}} = \frac{\sigma_e^{tr} - 3G\Delta p - \sigma_y - r}{3G + \frac{\partial r}{\partial \Delta p}} \tag{20a}$$

$$\Delta p = \Delta p^{tr} + d\Delta p \tag{20b}$$

So that the plastic strain tensor increment in Eq. (14) can be re-written

$$\Delta \varepsilon^p = \frac{3}{2}\, \Delta p \frac{\Delta p^{tr'}}{\sigma_e^{tr}} \tag{21}$$

Therefore, at the new time step the uncracked stress is updated as follows to return onto the new yield surface.

$$\sigma_{0_{t+\Delta t}} = E\left(\varepsilon_{t+\Delta t} - \left(\varepsilon^p{}_t + \Delta \varepsilon^p\right)\right) \tag{22}$$

Substituting the Eqs (20a,b), (21) into (22), the uncracked stress is re-written as

$$\sigma_{0_{t+\Delta t}} = E\left(\varepsilon_{t+\Delta t} - \left(\varepsilon_t^p + \frac{3}{2}\left(\Delta p^{tr} + \frac{\sigma_e^{tr} - 3G\Delta p - \sigma_y - r}{3G + \frac{\partial r}{\partial \Delta p}}\right)\frac{\Delta p^{tr'}}{\sigma_e^{tr}}\right)\right) \tag{23}$$

Eq. (23) is solved at the end of each time step for uncracked stress state, when is decomposed to tensile and compressive stresses to be used in Eq. (4a) is given by

$$\sigma_{t+\Delta t} = ((1 - \mathrm{c}_{t+\Delta t})^2(1-k) + k)\, \sigma_0^+{}_{t+\Delta t} + \sigma_0^-{}_{t+\Delta t} \tag{24}$$

where

$$c_{t+\Delta t} = \mathrm{c}_t + \frac{\partial c}{\partial t}\Delta t \tag{25}$$

Finally, the overall algorithm for coupling the elastic/plastic deformation with the phase-field is implemented in MOOSE (Gaston et al., 2015) (see Fig. 1) to solve for displacements and crack phase-field at each time step.

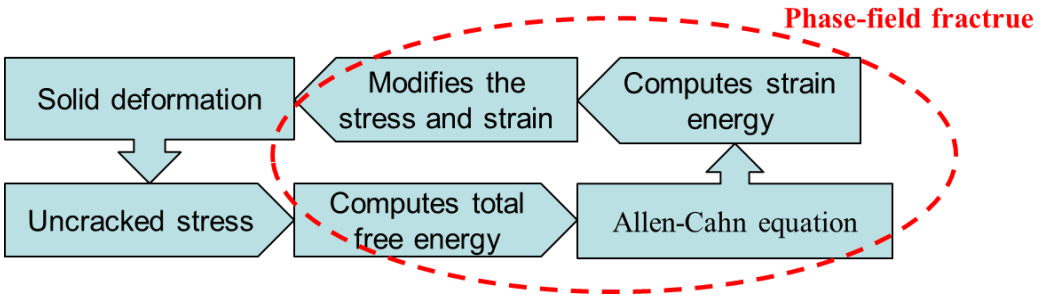

Fig. 1 The algorithm implemented in MOOSE to couple the elastic/plastic deformation and crack phase-field.

3 Punch Through Shear (PTS) test model

The stress concentrations at a fracture tip in rocks is determined by describing the fracture toughness in Mode I (opening) K_{IC}, Mode II (in-plain shear) K_{IIC}, and Mode III (out-of-plain shear) K_{IIIC} with respect to the far-field stress. The fracture toughness is a material parameter that depends on the physical boundary conditions such as confining pressure p_c (Meier, Backers, & Stephansso, 2009).

On the other hand, the critical energy release rate G_c is a material property and is independent of physical boundary conditions. Therefore, the value of critical energy release rate remains the same for any set of confining pressure. At no confining pressure, the Mode II fracture toughness can be obtained using the following relation.

$$K_{IIC} = \sqrt{E.G_C} \tag{26}$$

In this study, the punch through shear test (Backers et al., 2002; Kluge, Blöcher, Barnhoorn, & Bruhn, 2019) is applied on a cylindrical granite PGR6 sample with circular notches in the upper and lower surfaces (see Fig. 2). The center of the sample is remained intact before the test. In PTS-testing, the confining pressure was set to 40 MPa, when there was a pore pressure of 20 MPa within the rock matrix due to fluid flow. Consequently, the resulting effective pressure is 20 MPa. To simulate this stress state, as the fluid flow is not considered in numerical simulations, a confining pressure of 20 MPa is set to the lateral boundary condition. Therefore, the pore pressure was set to zero to resemble the condition of Terzaghi effective stress of 20 MPa in the experiment.

This test was developed to measure the Mode II fracture toughness, K_{IIc} of rock under different confining pressures. The axial load is exerted on the sample via uniaxial loading machine (see Fig. 2b). The details of the PTS-testing can be found in Kluge et al. (2019) and Backers et al. (2002). The load-displacement plot in Fig. 2a shows linear elastic behavior from the beginning of the test until 0.6 mm displacement, and plastic behavior from that point till the sample failure.

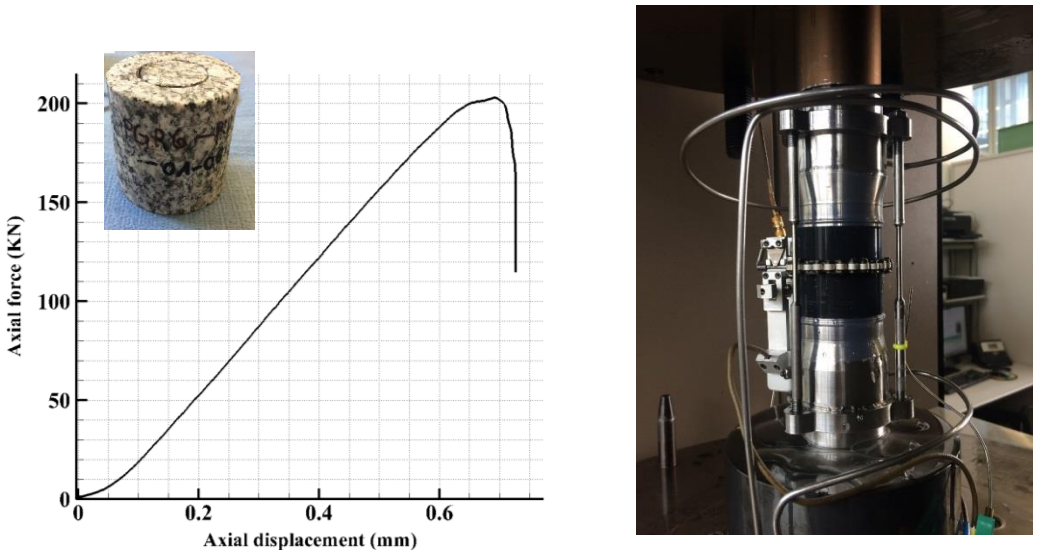

Fig. 2 a) Uniaxial load-displacement and granite sample PGR6, b) uniaxial setup (Kluge et al., 2019).

The numerical simulations were carried out to compute for the rock's yield stress and critical energy release rate. The numerical model is proposed according to the sample geometry, its dimensions, and the principal loading as are given in Fig. 3. The granite sample characteristics and dimensions are summarized in table 1.

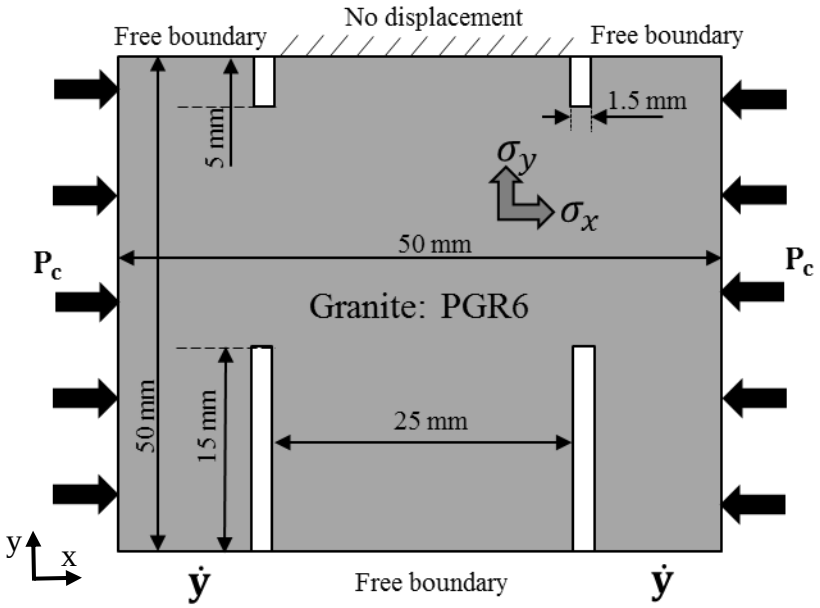

Fig. 3 Numerical model, dimensions, and boundary conditions.

Table 1 sample size and physical properties.

Material:	Granite: PGR6
Upper notch length (mm):	5
Lower notch length (mm):	15
Notch thickness (mm):	1
Intact length (mm):	30
Sample diameter (mm):	50
Elastic modulus E (GPa):	50
Poisson ratio ν (-):	0.2
Displacement rate, $\dot{\mathbf{y}}$ $\left(\frac{mm}{s}\right)$:	0.001
Confining pressure $p_c(MPa)$:	40

The finite element numerical code, built on the libMesh library of MOOSE (Gaston et al., 2015), computes for the rock's solid displacement-stress field (Eq. , u and the crack phase-field c in a time dependent simulations. The 2D axisymmetric model domain is discretized as shown in Fig. 4. The numerical results were obtained and compared to PTS-testing experimental results for the granite sample.

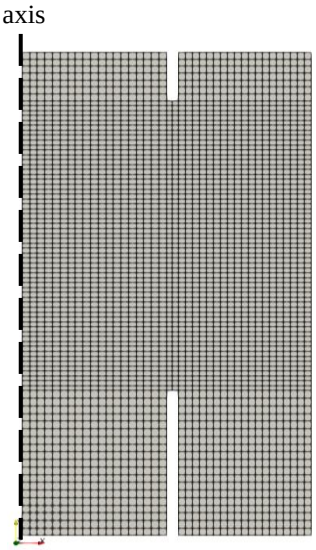

Fig. 4 2D axisymmetric computational grid consisting of 3348 quad elements and 85 boundary elements.

For the finite element computations, adoptive time step size is set with the maximum of $\Delta t_{max} = 0.2$ s, the cutback factor of 0.8, and the growth factor of 1.1. The computations are run until the point of the failure of the sample, where the time step size is reduced to $\Delta t = 10^{-15}$s. In current numerical simulations, the domain element size h is set to $h = 0.625$ mm, the regularization length l is set to $l = h$, and $h/2$. Other numerical parameters are set as follows in Table 2.

Table 2 Numerical parameters set in MOOSE script for four different simulations (*see* Eqs. (9) and (24)).

Parameter	**Simulation#1**	**Simulation#2**
Regularization length $l\ (mm)$	0.625	0.625
Elastic energy release rate $G_c\left(\frac{N}{m}\right)$	600	600
Yield stress $\sigma_y(MPa)$	375	300
Shear modulus $G(GPa)$	17.6	17.6
Small positive parameter $k(-)$	10^{-4}	10^{-4}
Parameter	**Simulation#3**	**Simulation#4**
Regularization length $l\ (mm)$	0.3125	0.625
Elastic energy release rate $G_c\left(\frac{N}{m}\right)$	600	250
Yield stress $\sigma_y(MPa)$	375	375
Shear modulus $G(GPa)$	17.6	17.6
Small positive parameter $k(-)$	10^{-4}	10^{-4}

4 Results and discussions

In the PTS-testing experiments of Kluge et al. (2019) and Backers et al. (2002), it was observed that at about 30 % of the peak load, a shear fracture (Mode II), known as the wing fracture, initiated from the bottom notch and propagated upwards to the intact zones of the rock. During propagation, the wing fracture oriented horizontally towards the center of the sample. In addition, Backers et al. (2002) reported that at about 60 % of the peak load, a small wing fracture initiated at the top notch. The small wing fracture (*i.e.* doughnut fracture) propagated outwards to the sides of the sample. However, there is a concern if the so-called doughnut fracture is not a Mode II fracture. Kluge et al. (2019) reported that the doughnut fracture was formed only due to the top notch walls collapse, thus, is not a shear mode fracture.

The growth of the wing fractures occur along with elastic deformation of the granite sample. This was seen in the linear behavior of the axial force-displacement plot until 0.6 mm axial displacement (*see* fig. 2a). The elastic deformation and the growth of the wing fractures within the sample continued until the sample underwent a plastic deformation starting from the axial displacement of $y = 0.6\ mm$ to $y = 0.675\ mm$. Finally, the sample failure occurred at the axial displacement of $y = 0.675\ mm$, when a new fracture initiated and propagated and connected the upper notch to the lower notch. In addition to the wing fracture and the fracture at failure,

In this study, the numerical model is implemented by applying the governing boundary conditions (Fig. 3) and the stress-displacement as well as fractures' initiation location and propagation directions were obtained from MOOSE phase-field solution. The crack phase-field parameter is set $c = 0$ throughout the domain as the initial condition. The crack phase-field parameter through time increases where the stress concentration occurs at the corners of the

lower and the upper notches until it gets a value of $c = 1$, which represents a fracture. In the numerical simulations, the input parameters were set as listed in table 2, simulation#1, and the corresponding results are shown in Figs 5, 6 and 7.

Fig. 5 shows the crack phase-field contours and the stress-displacement plot of the model domain at different loading times. As the lower surface of the sample is displaced upward with the rate of $\dot{y} = 0.001\ \mathrm{mm/s}$, similar to the PTS testing, the wing fractures initiated from the upper and the lower notches at time $t = 318\ \mathrm{s}$ with the axial displacement of $y = 0.318\ mm$ and propagated persistently toward the intact areas of the domain. The wing fractures initiation is shown in Fig. 5b where the stress-displacement is depicted in the corresponding plot in Fig. 5. It was observed that the wing fractures were propagated while the sample underwent the elastic deformation until $y = 0.6\ mm$ (*see* Figs 5c, 5d, and 5e). The plastic deformation of the model was seen from $y = 0.6\ mm$ until the sample failure at $y = 0.662\ mm$ (*see* Figs. 5f, 5g, and 5h). The sample failure is depicted at Fig. 5h where another fracture initiated and propagated between the upper and lower notches.

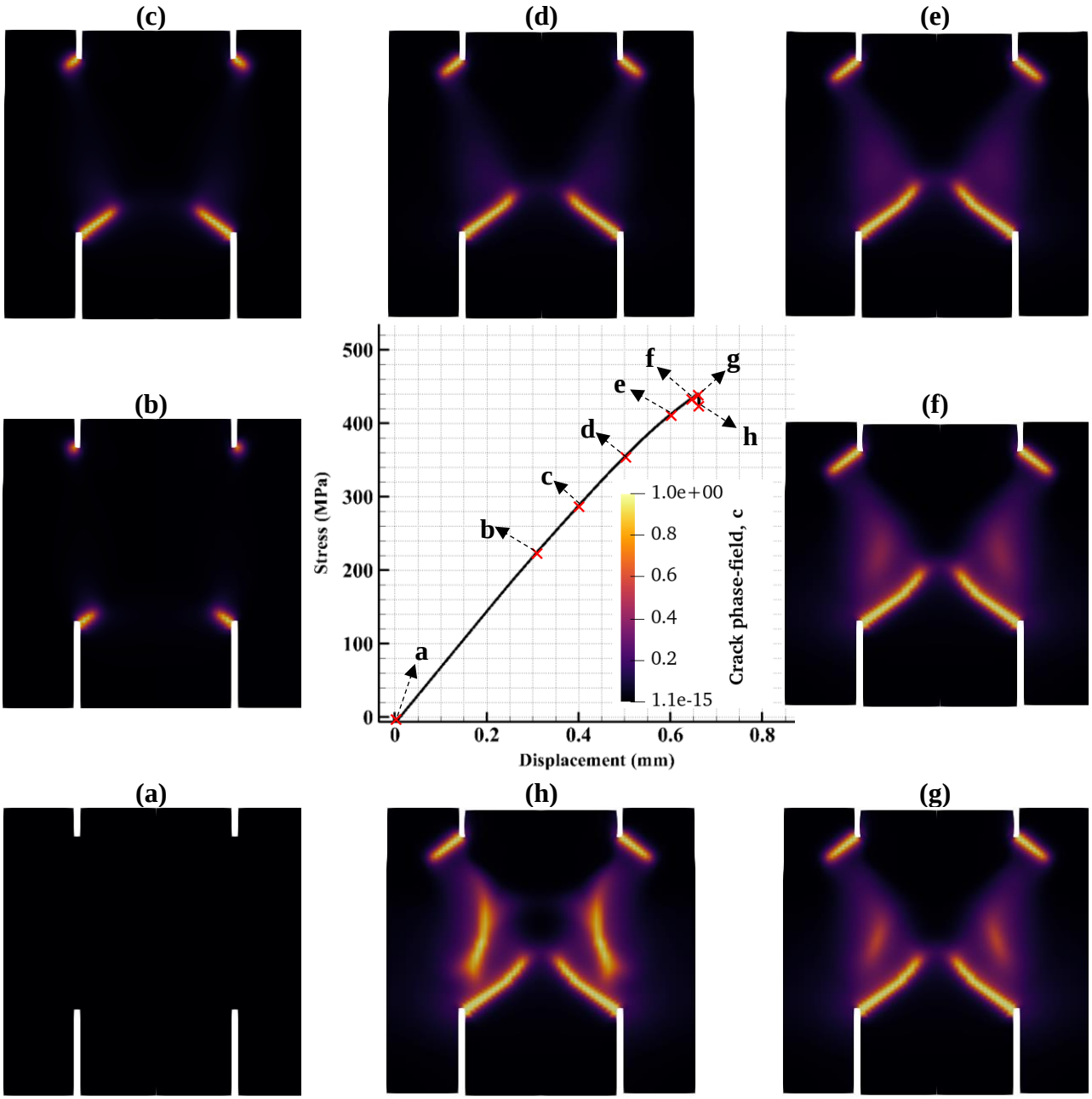

Fig. 5 Crack phase-field and domain stress-displacement (input parameters set as simulation#1) a) $t = 0\ s$, $y = 0\ mm$; b) $t = 318\ s$, $y = 0.318\ mm$ fractures initiation; c) $t = 400\ s$, $y = 0.4\ mm$; d) $t = 500\ s$, $y = 0.5\ mm$; e) $t = 600\ s$, $y = 0.6\ mm$, start of plastic fracturing; f) $t = 690$, $y = 0.65\ mm$; g) $t = 700\ s$, $y = 0.662\ mm$; h) $t = 702\ s$, $y = 0.662\ mm$, sample failure.

Fig. 6 shows the comparison between the numerical and experimental PTS X-ray CT scan at the rock failure. The wing fractures and the fracture at failure are highlighted with red lines across each fracture at the CT image.

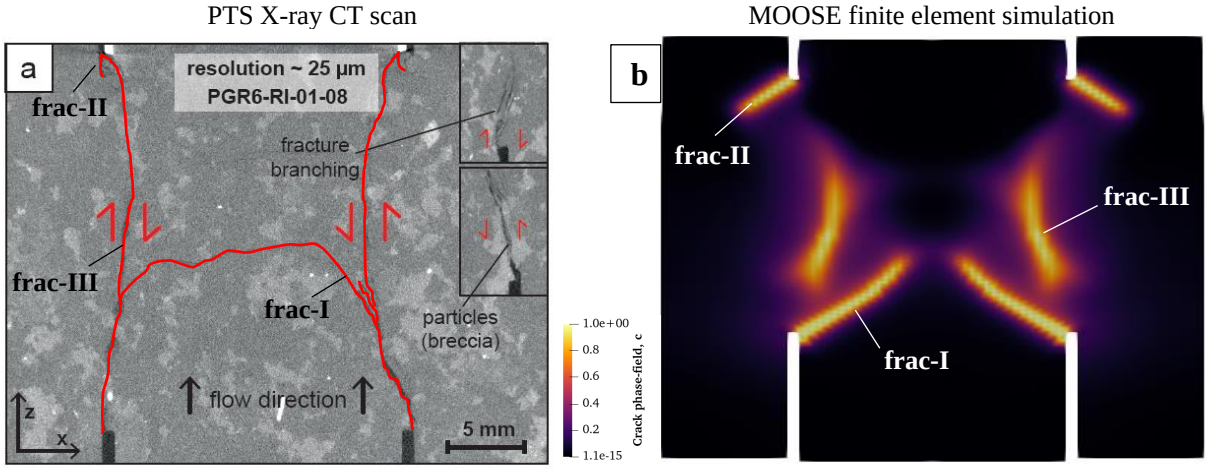

Fig. 6 Comparison between a) PTS-testing experimental CT-scan (Kluge et al., 2019) and b) MOOSE phase-field simulation at sample failure (displacement scale factor is 1).

Here, the fracture was initiated from the lower notch and propagated towards the center of the sample is called frac-I. Similarly, the fracture that was initiated from the upper notch (doughnut fracture) and propagated towards the sides of the sample is called frac-II. The fracture that appeared just at the sample failure connecting the upper notch and the lower notch is called frac-III (*see* Fig. 6a). The numerical phase-field simulation with MOOSE showed the initiation and propagation of the wing fractures, frac-I and frac-II until the sample failure, where frac-III was initiated and propagated towards the notches. However, the simulations near to the failure could not model the complete propagation of frac-III as the adoptive time step size became too small (*i.e.* 10^{-15}s) to show any further results due to the large strain rate.

Fig. 7 shows the distribution of the stress components within the sample along the line Γ. Line Γ with the length of 0.05128 m is selected to include all fractures at the rock failure state (*i.e.* the lower left side of the line Γ is accounted as 0). The stress concentration at the fracture tip at the presence of each frac-I, frac-II, and frac-III is depicted in Fig. 7 in the form of stress peaks. Fig. 7a shows the stress distribution along the line Γ at time $t = 359$ s where frac-II meets the line at the length of 0.045 m. It is noted that σ_{yy} is compressive (i.e. negative values) within the domain far from the notches, in the intact area. The closer to the fracture tip, the less compressive σ_{yy} is investigated. At the fracture tip, the stress component σ_{yy} shifts up to the maximum tensile stress $\sigma_{yy} = 0.3$ GPa (see Fig. 7a length of 0.045 m). Fig. 7b shows the stress distribution along line Γ at time $t = 420$ s, where frac-I met the line and frac-II has crossed the line. Here, the stress distribution curve shows two peaks indicating stress concentration at the vicinity of the wing fractures, frac-I and frac-II at the length of 0.018 m and 0.045 m, respectively. Fig. 7c shows the stress distribution at time $t = 700$ s, just before sample failure at 100% of leading (i.e. peak load). At this point, the maximum tensile stress is increased to $\sigma_{yy} = 1.7$GPa and 1.6GPa at the vicinity of frac-I and frac-II, respectively. Additionally, at this point of loading another fracture, frac-III, was initiating at the length of 0.027 m of the line Γ, where σ_{xx} and σ_{xy} get a peak value. Fig. 7d shows the stress distribution along line Γ at time of

sample failure (i.e. t = 702 s). Once the sample fails, the frac-III is initiated and grown at the length of 0.027 m on the line Γ. It is depicted as the stress concentration $\sigma_{yy} = 1.95$ GPa and $\sigma_{xx} = 1.55$ GPa. Furthermore, it is noted that after growth of frac-III, the tensile stress concentration at the vicinity of frac-I and frac-II is decreased. The comparison between the Fig. 7c and 7d shows that the stress concentration at the length of 0.045 m (i.e. where the frac-I exists on the line), $\sigma_{yy_{max}}$ reduces from 1.7 GPa to 1.15 GPa. This reduction in stress concentration is the result of energy loss due to plastic deformation of the rock.

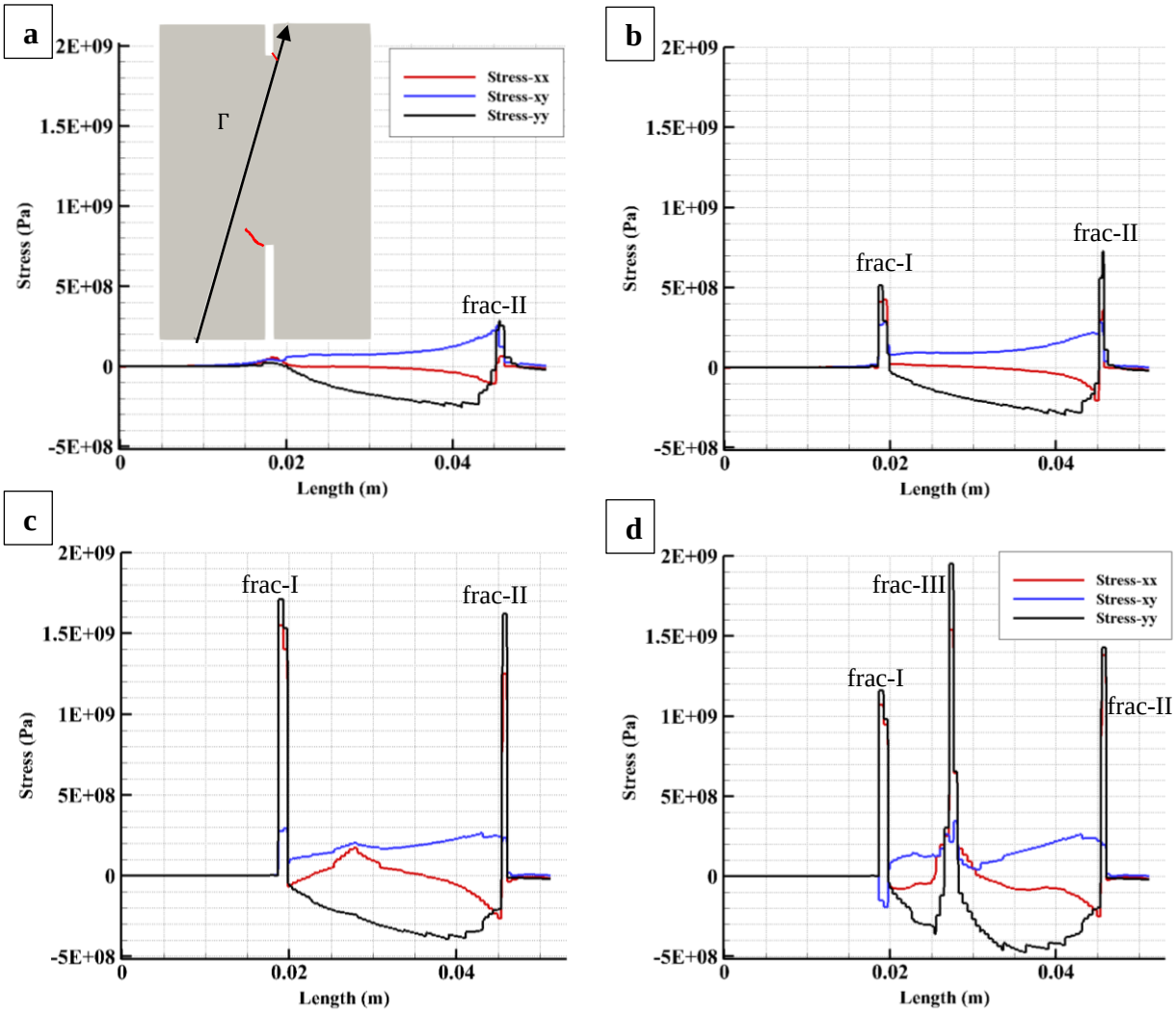

Fig. 7 Normal stresses and shear stress distribution along line Γ at a) time $t = 359s$, when the frac-II meets the line Γ, b) time $t = 420s$, when the frac-I meets the line Γ, c) time $t = 700s$, just before the sample failure, d) time $t = 702s$, at sample failure

For the validation purposes, the stress displacement curve, $\sigma_{yy} - y$ of the PTS testing experiments and the numerical simulations with the input parameters of simulation#1-4 (*see* table 2) are compared in Fig. 8. The simulation#1-4 show the calibration process for the current simulations. The effect of altering the parameters such as regularization length l, the elastic energy release rate G_c, yield stress σ_y, and shear modulus G on the stress-displacement plot is shown in Fig. 8. In numerical simulations, σ_{yy} is calculated at the model upper boundary.

Simulation#1 and experimental data showed the best agreement among other simulations, indicating that $G_c = 600$ N/m and $\sigma_y = 375$ MPa are the best selections for these material parameters. Other simulations showed earlier failure (simulation#4) or later failure (simulation#2, simulation#3) comparing to the experimental data. In addition, the elastic fracturing simulation result is depicted in blue dashed line for comparison with elastic-plastic fracturing curves.

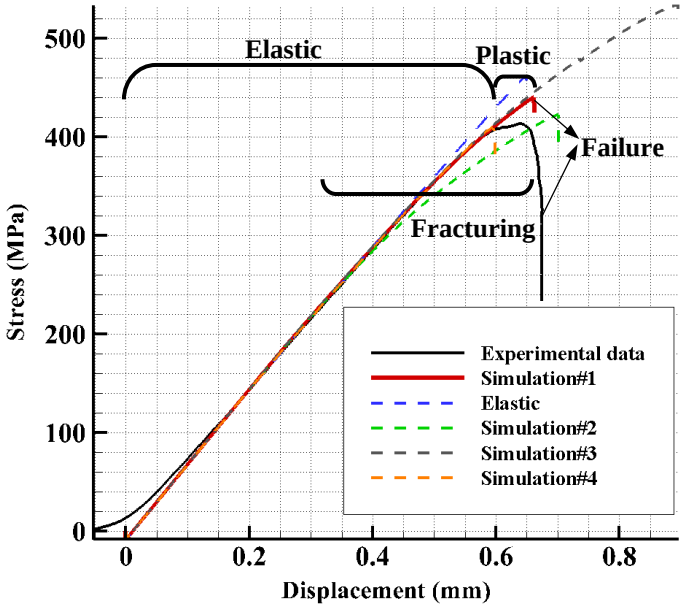

Fig. 8 Numerical validation against experimental results of Kluge et al. (2019) (*see* table 2 for different simulation).

At the axial displacement of $y = 0.318\ mm$, the fracturing occurred during elastic deformation of the rock as indicated in Fig. 8. At $y = 0.6\ mm$, the plastic deformation was observed through nonlinear behavior of stress-displacement curve of the experimental data and simulation#1. The fracturing during plastic deformation continues until failure as it is depicted in Fig. 8. The failure occurred at $y = 0.675\ mm$ in experimental data and with 1.9 % error at $y = 0.662\ mm$ in simulation#1.

According to the axial loading on the rock, the Mode II fracture is observed in numerical and experimental PTS-testing. Using Eq. (26) for no confining pressure, and $G_c = 600$ N/m from simulation#1, the Mode II fracture toughness of the granite rock sample is 4.85 MPa$\sqrt{\text{m}}$.

5 Conclusions

The critical energy release rate and the fracture toughness of granite rock sample was measured and calculated through the PTS-testing and the numerical simulation via MOOSE phase-field, respectively. The stress displacement curve of the PTS-testing showed the plastic deformation of the granite sample before sample failure. Therefore, the numerical model was carried out to model the fracture initiation and propagation, considering the rock's plastic behavior. The crack phase-field method was coupled to von Mises plasticity criterion, using radial return map plasticity algorithm. However, for elastic fracturing, the computations use the Hook's law to calculate the uncracked stress field and then update for cracked stress field, using

the crack phase-field parameter. The method was implemented on structured mesh with adoptive time step size that provided a computationally efficient and accurate numerical simulation, including elastic-plastic fracture initiation and propagation. The numerical results showed a good agreement in stress-displacement curve of experimental data for critical energy release rate of $G_c = 600\ N/m$. Therefore, the granite sample's fracture toughness for Mode II is calculated to be 4.85 $MPa\sqrt{m}$ at no confining pressure.

Acknowledgments, Samples, and Data

This study was supported by the Mitacs Globaling Research Award. The PTS-testing setup experiments and granite rock sample was provided by the GFZ research Centre for Geosciences in Potsdam, Germany. The stress displacement experimental data and numerical simulation results, as well as MOOSE script and numerical model, are provided through the University of Manitoba Library Dataverse (Jarrahi, 2020). Finally, authors would like to thank Dr. Mauro Cacace, from section "basin modelling" at GFZ, Potsdam, Germany for his helpful comments in writing the MOOSE script.

References

Affonso, L. O. A. (2006). 4 - Ductile and Brittle Fractures. In L. O. A. Affonso (Ed.), *Machinery Failure Analysis Handbook* (pp. 33-42): Gulf Publishing Company.

Allen, S. M., & Cahn, J. W. (1972). Ground state structures in ordered binary alloys with second neighbor interactions. *Acta Metallurgica, 20*(3), 423-433. doi:https://doi.org/10.1016/0001-6160(72)90037-5

Ambati, M., Gerasimov, T., & De Lorenzis, L. (2015). Phase-field modeling of ductile fracture. *Computational Mechanics, 55*(5), 1017-1040. doi:10.1007/s00466-015-1151-4

Areias, P., Msekh, M. A., & Rabczuk, T. (2016). Damage and fracture algorithm using the screened Poisson equation and local remeshing. *Engineering Fracture Mechanics, 158*, 116-143. doi:https://doi.org/10.1016/j.engfracmech.2015.10.042

Areias, P., Rabczuk, T., & Msekh, M. A. (2016). Phase-field analysis of finite-strain plates and shells including element subdivision. *Computer Methods in Applied Mechanics and Engineering, 312*, 322-350. doi:https://doi.org/10.1016/j.cma.2016.01.020

Backers, T., Stephansson, O., & Rybacki, E. (2002). Rock fracture toughness testing in Mode II—punch-through shear test. *International Journal of Rock Mechanics and Mining Sciences, Doctoral Thesis*.

Besson, J. (2009). Continuum Models of Ductile Fracture: A Review. *International Journal of Damage Mechanics, 19*(1), 3-52. doi:10.1177/1056789509103482

Bouchard, P. O., Bay, F., & Chastel, Y. (2003). Numerical modelling of crack propagation: automatic remeshing and comparison of different criteria. *Computer Methods in Applied Mechanics and Engineering, 192*(35), 3887-3908. doi:https://doi.org/10.1016/S0045-7825(03)00391-8

Bourdin, B., Francfort, G. A., & Marigo, J. J. (2000). Numerical experiments in revisited brittle fracture. *Journal of the Mechanics and Physics of Solids, 48*(4), 797-826. doi:https://doi.org/10.1016/S0022-5096(99)00028-9

Crété, J. P., Longère, P., & Cadou, J. M. (2014). Numerical modelling of crack propagation in ductile materials combining the GTN model and X-FEM. *Computer Methods in Applied Mechanics and Engineering, 275*, 204-233. doi:https://doi.org/10.1016/j.cma.2014.03.007

Davies, J. W., & Wells, A. A. (1961). Cleavage Fracture Initiation in Notched Impact Tests of Mild Steel. *Nature, 190*(4774), 432-432. doi:10.1038/190432a0

Dawicke, D. S., Piascik, R. S., & Newman, J. C. (1997). Prediction of Stable Tearing and Fracture of a 2000-Series Aluminum Alloy Plate Using a CTOA Criterion. In R. S. Piascik, J. C. Newman, & N. E. Dowling (Eds.), (pp. 90-104). West Conshohocken, PA: ASTM International.

Dittmann, M., Aldakheel, F., Schulte, J., Wriggers, P., & Hesch, C. (2018). Variational phase-field formulation of non-linear ductile fracture. *Computer Methods in Applied Mechanics and Engineering, 342*, 71-94. doi:https://doi.org/10.1016/j.cma.2018.07.029

Dunne, F., & Petrinic, N. (2005a). *Introduction to Computational Plasticity*: Oxford University Press.

Dunne, F., & Petrinic, N. (2005b). *Introduction to Computational Plasticity*: Oxford University Press on Demand.

Elices, M., & Liorca, J. (2002). MODELS OF FIBRE FRACTURE. In M. Elices & J. Llorca (Eds.), *Fiber Fracture* (pp. 27-56). Oxford: Elsevier Science Ltd.

Gaston, D. R., Permann, C. J., Peterson, J. W., Slaughter, A. E., Andr, D., Wang, Y., . . . Martineau, R. C. (2015). Physics-based multiscale coupling for full core nuclear reactor simulation. *Annals of Nuclear Energy, 84*, 9.

Hofacker, M., & Miehe, C. (2012). A Phase Field Model for Ductile to Brittle Failure Mode Transition. *PAMM, 12*(1), 173-174. doi:10.1002/pamm.201210077

Huang, C., & Gao, X. (2019). Development of a phase field method for modeling brittle and ductile fracture. *Computational Materials Science, 169*, 109089. doi:https://doi.org/10.1016/j.commatsci.2019.109089

Hussain, M. A., Pu, S. L., & Underwood, J. (1974). Strain Energy Release Rate for a Crack Under Combined Mode I and Mode II. In G. R. Irwin (Ed.), (pp. 2-28). West Conshohocken, PA: ASTM International.

James, M. A., & Newman, J. C. (2003). The effect of crack tunneling on crack growth: experiments and CTOA analyses. *Engineering Fracture Mechanics, 70*(3), 457-468. doi:https://doi.org/10.1016/S0013-7944(02)00131-5

Jarrahi, M. (2020). Manitoba Population Research Data Repository, MOOSE phase-field. doi:https://doi.org/10.5203/FK2/JWQE5B, https://dataverse.lib.umanitoba.ca/dataverse/HFMiad

Johnson, G. R., & Stryk, R. A. (1987). Eroding interface and improved tetrahedral element algorithms for high-velocity impact computations in three dimensions. *International Journal of Impact Engineering, 5*(1), 411-421. doi:https://doi.org/10.1016/0734-743X(87)90057-1

Karihaloo, B., & Xiao, Q. Z. (2003). 2.03 - Linear and Nonlinear Fracture Mechanics. In I. Milne, R. O. Ritchie, & B. Karihaloo (Eds.), *Comprehensive Structural Integrity* (pp. 81-212). Oxford: Pergamon.

Kluge, C., Blöcher, G., Barnhoorn, A., & Bruhn, D. (2019). *Hydraulic-mechanical characterisation of microfaults in granite – an experimental study*. Paper presented at the 13th Euro-conference on rock physics and Geomechanics the GUEGUEN conference, Potsdam, Germany.

Kuhn, C., & Müller, R. (2008). A phase field model for fracture. *PAMM, 8*(1), 10223-10224. doi:10.1002/pamm.200810223

Kuhn, C., & Müller, R. (2010). A continuum phase field model for fracture. *Engineering Fracture Mechanics, 77*(18), 3625-3634. doi:https://doi.org/10.1016/j.engfracmech.2010.08.009

Lei, Q., & Wang, X. (2016). Tectonic interpretation of the connectivity of a multiscale fracture system in limestone. *Geophysical Research Letters, 43*(4), 1551-1558. doi:10.1002/2015gl067277

Madenci, E., & Oterkus, E. (2014). *Peridynamic Theory and Its Applications*. New York: Springer Science+Business Media.

Mahmoud, S., & Lease, K. (2003). The effect of specimen thickness on the experimental characterization of critical crack-tip-opening angle in 2024-T351 aluminum alloy. *Engineering Fracture Mechanics, 70*(3), 443-456. doi:https://doi.org/10.1016/S0013-7944(02)00130-3

Maiti, S. K., & Smith, R. A. (1984). Comparison of the criteria for mixed mode brittle fracture based on the preinstability stress-strain field. *International Journal of Fracture, 24*(1), 5-22. doi:10.1007/BF00020264

McClintock, F. A. (1963). Discussion: “On the Crack Extension in Plates Under Plane Loading and Transverse Shear” (Erdogan, F., and Sih, G. C., 1963, ASME J. Basic Eng., 85, pp. 519–525). *Journal of Fluids Engineering, 85*(4), 525-527. doi:10.1115/1.3656898

Meier, T., Backers, T., & Stephansso, O. (2009). *The Influence of Temperature On Mode II Fracture Toughness Using the Punch-Through Shear With Confining Pressure Experiment*. Paper presented at the ISRM International Symposium on Rock Mechanics - SINOROCK 2009, The University of Hong Kong, China. https://doi.org/

Miehe, C., & Mauthe, S. (2016). Phase field modeling of fracture in multi-physics problems. Part III. Crack driving forces in hydro-poro-elasticity and hydraulic fracturing of fluid-saturated porous media. *Computer Methods in Applied Mechanics and Engineering, 304*, 619-655. doi:https://doi.org/10.1016/j.cma.2015.09.021

Miehe, C., Welschinger, F., & Hofacker, M. (2010). Thermodynamically consistent phase-field models of fracture: Variational principles and multi-field FE implementations. *International Journal for Numerical Methods in Engineering, 83*(10), 1273-1311. doi:10.1002/nme.2861

Mouritz, A. P. (2012). Introduction to Aerospace Materials. In A. P. Mouritz (Ed.), *Introduction to Aerospace Materials* (pp. 428-453): Woodhead Publishing.

Nam, H. S., Kim, J. S., Han, J. J., Kim, J. W., & Kim, Y. J. (2014). Ductile fracture simulation for A106 Gr.B carbon steel under high strain rate loading condition. In L. Ye (Ed.), *Recent Advances in Structural Integrity Analysis - Proceedings of the International Congress (APCF/SIF-2014)* (pp. 37-41). Oxford: Woodhead Publishing.

Peerlings, R. H. J., DE Borst, R., Brekelmans, W. A. M., & DE Vree, J. H. P. (1996). Gradient enhanced damage for quasi-brittle materials. *International Journal for Numerical Methods in Engineering, 39*(19), 3391-3403. doi:10.1002/(sici)1097-0207(19961015)39:19<3391::aid-nme7>3.0.co;2-d

Pineau, A., & Besson, J. (2001). SECTION 7.8 - Ductile Rupture Integrating Inhomogeneities in Materials (DRIIM). In J. Lemaitre (Ed.), *Handbook of Materials Behavior Models* (pp. 587-596). Burlington: Academic Press.

Rabczuk, T., & Belytschko, T. (2004). Cracking particles: A simplified meshfree method for arbitrary evolving cracks. *International Journal for Numerical Methods in Engineering, 61*(13), 26.

Ren, H., Zhuang, X., Cai, Y., & Rabczuk, T. (2016). Dual-horizon peridynamics. *International Journal for Numerical Methods in Engineering, 108*(12), 1451-1476. doi:10.1002/nme.5257

Rice, J. R. (1968). A Path independent integral and the approximate analysis of strain concentration by notches and cracks. *Journal of Applied Mechanics, 35*, 7.

Speight, J. G. (2016). *Handbook of Hydraulic Fracturing*: John Wiley and Sons.

Sukumar, N., Moës, N., Moran, B., & Belytschko, T. (2000). Extended finite element method for three-dimensional crack modelling. *International Journal for Numerical Methods in Engineering, 48*(11), 1549-1570. doi:10.1002/1097-0207(20000820)48:11<1549::aid-nme955>3.0.co;2-a

Rock Failure Mechanisms: Explained and Illustrated (2010).

Ulmer, H., Hofacker, M., & Miehe, C. (2013). Phase Field Modeling of Brittle and Ductile Fracture. *PAMM, 13*(1), 533-536. doi:10.1002/pamm.201310258

Zhang, J.-S. (2010). High Temperature Deformation and Fracture of Materials.